

# Ambient Noise Rayleigh Wave Tomography of New Zealand

Fan-Chi Lin<sup>1</sup>, Michael H. Ritzwoller<sup>1</sup>, John Townend<sup>2</sup>, Martha Savage<sup>2</sup>, Stephen Bannister<sup>3</sup>

1 - Center for Imaging the Earth's Interior  
Department of Physics  
University of Colorado at Boulder  
Boulder, CO 80309-0390 USA  
[linf@ciei.colorado.edu](mailto:linf@ciei.colorado.edu), (303 492 0985)

2- Victoria University of Wellington  
Institute of Geophysics  
Box 600  
Wellington, 6001 NZ

3- Institute of Geological and Nuclear Sciences  
69 Gracefield Rd.  
PO Box 30-368  
Lower Hutt, NZ

In preparation for submission to *Geophysical Journal International*, July, 2006.

## **Abstract**

### **1. Introduction**

Surface wave tomography has proven to be very useful in imaging Earth's crust and uppermost mantle on both regional and global scales across much of the globe. Surface waves at different periods are sensitive to seismic shear wave speeds at different depths, with the longer period waves exhibiting sensitivity to greater depths. By measuring the dispersive character of surface waves, strong constraints can be placed on the structure of the crust and upper mantle. Information derived from the study of surface wave studies would be useful to help improve the understanding of the tectonic architecture of New Zealand, but few studies of surface waves currently exist. This results, in part, from the historical shortage of broad-band seismic stations in New Zealand (which has been largely rectified now by GeoNet), but more fundamentally derives from basic limitations suffered by earthquake-based surface wave tomography. For example, in regions like New Zealand with relatively low seismicity, surface wave dispersion measurements derive nearly exclusively from teleseismic earthquakes. It is difficult to obtain reliable short-period (<20 sec) dispersion measurements from distant events due to intrinsic attenuation and scattering along ray paths. It is, however, the short-period waves that are most useful to constrain the structure of the crust and uppermost mantle. In addition, surface wave sensitivity functions for teleseismic events are spatially broad, which limits lateral resolution. For these reasons, the long history of multidisciplinary research on the

structure and tectonics of New Zealand (recent examples include Davey, 1998; Stern et al., 2000; Okaya et al., 2002; Scherwath et al., 2002; Savage et al., 2004; Baldock and Stern, 2005; Reyners et al., 2006; Stern, 2006) remains largely uninformed by studies of seismic surface waves.

Some of the problems that affect traditional teleseismic earthquake surface wave tomography can be alleviated by observations made on diffuse wavefields (e.g., ambient noise, scattered coda waves). Theoretical studies have shown that, under the right circumstances, the time-derivative of the cross-correlation of records from two seismic stations provides an estimate of the Green function between the stations, modulated by the spectrum of the noise source (Weaver and Lobkis, 2001a, 2001b, 2004; Derode et al., 2003; Snieder, 2004; Wapenaar, 2004; Larose et al., 2005). Seismic observations have confirmed the theory using both coda waves (Campillo and Paul, 2003; Paul et al., 2005) and ambient noise for surface waves (Shapiro and Campillo, 2004; Sabra et al., 2005a) and crustal body waves (Roux et al., 2005). Oceanic applications also appear to be feasible (Lin et al., 2006). The method has been applied successfully to stations in Southern California to obtain high-resolution surface wave tomography maps at short periods ranging from 7.5 to 15 sec (Shapiro et al., 2005; Sabra et al., 2005b). The group velocity maps from these studies show a striking correlation with the geological units in California with low-speed anomalies corresponding to the principal sedimentary basins and high-speed anomalies corresponding to the igneous cores of the major mountain ranges. Similar results have been established on a larger scale and have been extended to longer periods across much of Europe (Yang et al., 2006). Other applications have arisen across all of California and the Pacific Northwest while tracking the growth of the Transportable Array component of EarthScope (Moschetti et al., 2005), in South Korea at

very short periods (Cho et al., 2006), in Tibet at long periods (Yao et al., 2006), and elsewhere in the world.

New Zealand is a prime target for ambient noise surface wave tomography. It is now spanned by a modern broad-band seismological network (GeoNet, Fig. 1) and it is surrounded on all sides by sea. This oceanic isolation, which subjects it to some of the most sustained and energetic ocean waves on Earth (e.g., Laing et al., 2000; Gorman et al., 2003), creates very high ambient noise levels that can be exploited for ambient noise tomography and which suggest the possibility of a more uniform illumination of the crust than elsewhere in the world.

In this paper we apply ambient noise tomography between 6 sec and 30 sec period to 42 broad-band seismic stations distributed almost evenly across the North and South islands of New Zealand (Fig. 1). The data processing procedure that we apply is described in detail by Bensen et al. (2006) and is summarized briefly in section 2 here. One of the principal benefits of ambient noise tomography over traditional earthquake tomography is the ability to estimate measurement uncertainties based on the repeatability of the measurements. The error analysis and its use to identify reliable measurements is described in section 3. The tomography for group speed maps between periods of 8 sec and 23 sec is presented in section 4 and section 5 discusses the apparent azimuthal distribution of ambient noise sources that form the basis for the tomography. We close in section 6 with several regionalized inversions for crustal shear wave speeds consistent with the tomographic maps and also discuss the geological correlation and significance of the features in the maps.

## 2. Data processing and group velocity measurements

We compiled continuous vertical-component seismic data from 42 stations from the GeoNet project and the Global Seismic Network (GSN) (Fig. 1) over the last 9 months of 2005 and first 3 months of 2006. Use of vertical-components limits analysis to Rayleigh waves. Bensen et al. (2006) discuss at length the data processing scheme that precedes ambient noise tomography and we make only minor modifications here. We briefly summarize the method and indicate the modifications.

Data are processed one day at a time and divide into single-station and station-pair processing. Single station processing begins by band-pass filtering the data in the period band from 5 to 150 sec after the daily trend, the mean and the instrument response have been removed. Unwanted events such as earthquake signals and instrumental irregularities are removed by what we call temporal normalization in which we weight the waveform by the inverse of the average of the envelope function taken within a moving window that is 128 sec in duration. In fact, although the weights are applied on the raw seismogram, they are computed on the seismogram that has been band-pass filtered between 15 to 50 sec period. This band contains the most energetic part of the surface waves arriving after earthquakes. Although New Zealand itself is not strongly seismic, earthquakes occur regularly along the Tonga-Kermadec trench to the north, so cross-correlations between stations in New Zealand tend to be contaminated by earthquakes, which appear on cross-correlations as precursory arrivals. Bensen et al. (2006) show how tuning the temporal normalization to regional earthquake conditions

can help to diminish such spurious arrivals. Signals are then whitened in the frequency domain and band-pass filtered in the period band from 5 to 100 sec. Waveforms from each station-pair are cross-correlated on a daily basis and then added to produce one 12-month stack and 12 three-month stacks. The three-month stacks are used to estimate the uncertainty of the dispersion measurements, which is discussed further in the section 3.

**Figure 2** shows an example of 12-month stacks of broad-band (5 to 100 sec) cross-correlations plotted as a record-section with station BFZ (location name?) at the center. Clear signals are seen on both positive and negative correlation lags with physically reasonable move-outs (2-3 km/sec). The signals at positive and negative lags sample the same media. For this reason, we average the positive and negative lag signals into what is called the “symmetric-component. **Figure 3** displays 12-month symmetric-component cross-correlations between the stations DSZ (location name?) and HIZ (location name?). The earlier arrivals at longer periods result from the normal dispersion of the signals in which the longer periods travel faster than the short periods. **Figure 4a** compares a broad-band cross-correlation with its symmetric-component for the station-pair EAZ (location name?) and THZ (location name?)

As in earthquake dispersion analysis (e.g., Ritzwoller and Levshin, 1998), the dispersion measurement applied to ambient noise cross-correlations is based on Frequency-Time Analysis (FTAN) in a two-step process. However, the procedure applied here is automated whereas the earthquake analysis involves interaction by an analyst. Bensen et al. (2006) also discuss the dispersion measurement procedure in greater detail,

and here we provide only a brief summary. In the first step, traditional FTAN creates a two-dimensional diagram of signal power as a function of time and the central frequency of the applied filters (Fig. 4c). The automatic procedure tracks the local power maximum along the frequency axis. The group arrival times of the maximum amplitude as a function of filter frequency are used to calculate the tentative (raw) group velocity curve. Formal criteria are set to reject curves with distinctly irregular behavior or to interpolate through small spectral holes by selecting realistic local instead of absolute maxima. The second part of the method is the application of a phase-matched or anti-dispersion filter (Fig. 4d). In the non-automated method that has been applied to large numbers of earthquake signals, the analyst defines both the phase-matched filter and the frequency band of the measurement. In the automated method used here, the frequency band of measurement is pre-set and the phase-matched filter is defined by the dispersion curve that results from the first step of the process. In both the traditional and automated analyses, the actual frequency of a given filter is found from the phase derivative of the output at the group time of the selected amplitude maximum (Levshin and Ritzwoller, 2001). Bensen et al. (2006) also discuss the method to measure phase velocities, but only group velocities are used in the present paper.

We break from the method of analysis advocated by Bensen et al. (2006) principally in that we found that if we performed the phase-matched filtering procedure in four overlapping period bands (5s-14s, 10s-25s, 15s-35s, 20s-50s) we would increase the number of measurements. This is because even though spectral whitening is applied to the single-station data, the spectra of the cross-correlations are not white, but are stronger in some bands than others. Breaking the dispersion analysis into sub-bands effectively

flattens the amplitude spectra and improves the measurements in many cases. The dispersion curves at the edges of each period band, however, do not match perfectly. This is why the period bands overlap, and in regions of over-lap we choose measurements that give the lowest average standard deviation of group velocity among the 3-month stacks. We discuss this further in section 3.

**Figure 5b** shows four group speed curves between the station-pairs DCZ-LTZ, OUZ-QRZ, KHZ-ODZ and PXZ-WCZ with paths through four distinct geological regions shown in **Figure 5a**. The curves do not meet seamlessly between the four frequency bands in which they are measured. In general, a Rayleigh wave samples to the depth of about one-third of a wavelength. Low wave speeds at short periods (<15s) usually indicate sediments near the surface and high wave speeds usually are associated with the igneous cores of mountain ranges or highly metamorphosed terrains. The lowest wave speeds at short periods in **Figure 5b** are for the path OUZ-QRZ due to off-shore sediments. On the other hand, at longer periods, waves begin to sample the upper mantle and a relatively short period onset of high group speeds is related to thin crust because the high-speed mantle is nearer to the surface. The off-shore path OUZ-QRZ path is also fastest at the long period end of **Figure 5b**. due to thinner crust off-shore. In general, the slope of the dispersion curve from about 20 – 30 sec provides information about crustal thickness. Note that the DCZ-LTZ path is through the Southern Alps, an area considered to have the thickest crust in New Zealand, and has the flattest group speed curves between 20 – 30 sec period.



### 3. Error analysis and data selection

The automated measurement procedure must be followed by the application of criteria to select reliable measurements. We apply four general types of criteria: (1) a period cut-off related to inter-station distance, (2) signal-to-noise ratio (SNR), (3) repeatability of the measurements (particularly seasonal variability), and (4) coherence across the set of measurements. The formal uncertainty analysis is based on seasonal variability.

First, for short distance station-pairs, the signals at positive and negative lags can interfere with each other at long periods which renders the measurements unreliable. This effect can be mitigated by introducing a period cut-off in which measurements are accepted only if the inter-station distance is greater than  $\sim 3$  wavelengths. A phase speed of  $\sim 4$  km/sec provides a rule-of-thumb in which we will accept a measurement only below the cut-off period of  $\Delta/12$  sec, where  $\Delta$  is the inter-station distance in kilometers. Experience shows that this is near the period where measurements become decreasingly reliable, being less repeatable and more subject to changes due to small variations in the measurement process.

Second, the quality of the dispersion measurement is highly correlated with the signal-noise-ratio (SNR) of the cross-correlation. We compute spectral SNR by applying a series of narrow band-pass filters and measuring signal-to-noise levels after returning to the time-domain. The signal level is the peak in the arrival window and the noise level is the root-mean-square (rms) noise in the noise window. The arrival window is defined by the expected Rayleigh wave group times taken from the 3-D model of Shapiro and

Ritzwoller (2002) at the minimum and maximum periods of the pass-band expanded by 75 sec in both directions. The noise window starts 500 sec after the end of the signal window and ends at 2700s lag time. [Figure 4b](#) shows examples of spectral SNR for the positive and negative lag signals in [Figure 4a](#) and compares with the SNR of the symmetric-component. The highest SNR is on the positive-lag in this case. The symmetric-component is not much degraded in SNR compared with the positive-lag, which is one of the reasons we use it to obtain the dispersion measurements. SNR is typically highest at the New Zealand stations below about 20 sec period which is in the microseism band, and drops rapidly at periods above about 25 sec. This is one of the reasons why the analysis in this paper concentrates at periods below 30 sec. The other principal reason is that a 30 sec dispersion measurement, as discussed in the previous paragraph, will require an inter-station spacing of 480 km. Such long paths are exclusively along the strike of New Zealand, and azimuthal coverage above about 20 sec period is not as good as at shorter periods where shorter paths can be used.

Third, we demand that the measurement be repeatable to be selected for tomography. To quantify repeatability, we use the seasonal variability of the measurements and then equate this to measurement uncertainties. We accept a measurement only if the uncertainty is well defined and below a specified threshold. To compute seasonal variability, we utilize the twelve 3-month stacks (Jan-Feb-Mar, Feb-Mar-Apr, ..., Dec-Jan-Feb) and the dispersion curves measured from them. [Figure 6](#) presents an example. For each period and station-pair, if there are more than seven 3-month stacks with a SNR higher than 15, we consider these as potentially good measurements. We then compute the standard-deviation (STD) of group speed and arrival time using those

three-month stacks. We screen out all the station-pairs with either a STD of group speed higher than 100m/s or a STD of arrival time that is higher than 4 sec. The results for the average STD of group velocity for the four period bands we use in the dispersion measurement process are plotted in [Figure 7](#). The uncertainties increase at the edges of each period band. For periods covered by more than one period band, the data from the band giving the smaller uncertainty is chosen. For example, for 21 sec period, the band from 15s to 35s gives the lower average STD group velocity and it is this band that is chosen to provide the 21 sec measurement. The instability of the STD at periods longer than 30 sec is caused by a small number of measurements, as shown in [Fig 8a](#).

If a measurement satisfies the first three selection criteria, we call the cross-correlation an “estimated Green function”. The number of measurements that satisfy these criteria, the average SNR, the average uncertainty of group speed and the average uncertainty of the arrival time at each period are summarized in [Figure 8](#). Note that above 25 sec period, very few measurements pass the selection criteria which limits tomography to periods below this threshold. [Figure 9](#) plots all the paths satisfying these criteria at 8, 13, 18 and 23 sec period. At the longer periods, ray-paths are increasingly confined to paths along the spines of the islands due to the 3-wavelength inter-station spacing criterion. Paths transverse to the strike of the islands exist in fairly large numbers at 8 sec period and also at 13 sec period.

#### 4. Group speed tomography

The dispersion measurements of Rayleigh waves from one-year cross-correlations are used to invert for group velocity maps on a  $0.25^\circ \times 0.25^\circ$  grid across New Zealand and the surrounding sea using the tomographic method of Barmin et al. (2001). This method is based on minimizing a penalty functional composed of a linear combination of data misfit, model smoothness and the perturbation  $\mathbf{m}$  to a reference model  $\mathbf{m}_0$  for isotropic wave speed. Measurement uncertainties are used in the inversion. In regions of poor data coverage, the estimated model blends smoothly into the reference model. No adequate reference crustal model exists on the scale of this experiment, so the average of the measurements specifies  $\mathbf{m}_0$ . A more detailed discussion of this method is given by Barmin et al. (2001) and another recent application can be found in Yang et al. (2006).

Damping parameters weight the relative influence of data fit, smoothing, and tendency to merge the estimated model into the background model. The choice of these parameters is subjective. We perform a series of tests using different combinations of these parameters to determine acceptable values by considering data misfit, model resolution, and model norm. Ray theory is used to compute the travel times of surface waves. In recent years, surface wave studies have increasingly moved toward diffraction tomography using spatially extended finite-frequency sensitivity kernels based on the Born/Rytov approximation (e.g. Clevede et al. 2000; Spetzler et al., 2002; Ritzwoller et al., 2002; Yoshizawa & Kennett, 2002, Zhou et al., 2004; many others). Ritzwoller et al. (2002) showed that diffraction tomography recovers similar structure to ray theory at periods shorter than 50 sec in most continental regions. In the context of regional

tomography with dense path coverage, Sieminski et al. (2004) showed that nearly identical resolution can be achieved using ray theory as that using finite-frequency theory. In this study, we concentrate at short periods and on New Zealand where station coverage and the resulting ray paths are both dense, so that ray theory suffices for surface wave tomography. Dahlen and Zhou (2006) caution that group delay tomography for group speeds suffers from a simultaneous sensitivity to phase speeds, but this poses only a potential problem at much longer periods than considered here.

Resolution is estimated using the method described by Barmin et al. (2001) with modifications presented by Levshin et al. (2005). Each row of the resolution matrix is a resolution surface (or kernel), which is a map defining the resolution at one spatial node. We summarize information in the resolution surface by a single scalar quantity at each node, called the spatial resolution. Because the shape of the resolution surface for most nodes resembles a 2-D spatial Gaussian function, we fit a 2-D symmetric spatial Gaussian function to the surface at each node. The spatial resolution at each node is summarized by the standard deviation  $\gamma$  parameter of the best-fit Gaussian function to the resolution map. The resolution estimated across the region of study at periods of 8, 13, 18 and 23 sec is shown in Fig. 10. Resolution is fairly constant from 8 to 18 sec period, and averages about 35 km, approximately half the inter-station spacing as expected for good data coverage. Because few measurements span the two islands at 8 sec period, however, resolution between the islands at 8 sec is worse than at longer periods. By 23 sec period, resolution has degraded relative to shorter periods because the number of measurements is less and also because the number of paths transverse to the strike of the islands is reduced.

The result of the tomography for 8, 13, 18 and 23 sec is shown in Fig. 11. Rayleigh wave speeds on the South Island are typically faster than on the North Island. At 13 sec period, the fastest speeds can be seen in the western South Island and wave speeds are typically more variable on the North Island than the South Island. The lowest wave speeds are found off-shore, west of the North Island. The worse resolution at 23 sec period results in smoother tomographic features. Further discussion of the geological correlation of these features is found in section 6.

The fits that the group speed maps provide to the data are shown in Fig. 12. These histograms show the misfit for all the data that passed the first three selection criteria discussed in section 3. The standard-deviation of each distribution is also presented on the figure. The reduction in variance (relative to the average across each map) at 8, 13, 18, and 23 sec period is 92%, 92%, 80%, and 88%, respectively. The final step in data selection (Step 4 in section 3) is the attempt to use only measurements that agree with the data set as whole. This involves iteratively rejecting badly fit measurements.

Measurements with misfit larger than 7 sec, therefore, are removed prior to obtaining the final maps shown in Figure 11. The first three steps in the data selection removed nearly all of the bad measurements, and this final step removes only a few measurements and has only a minimal affect on the ultimate maps.

## 5. Azimuthal distribution of ambient noise sources

The cross-correlation not only contains information about the wave propagation characteristics between the station-pair (e.g., Rayleigh wave speed), but also can provide information about the azimuthal distribution of the source(s) of ambient noise. Further consideration of the positive and negative lags of the cross-correlation can provide insight into the relative strength of the waves that have propagated in the opposite directions between the two stations. The results presented here are for the 12-month stacks and, therefore, represent a yearly average. There may be seasonal variability that is not presented in these results.

To use this information, we calculate the SNR spectrum for the positive and negative lag components of the cross-correlation between each station-pair and multiply that by the square root of the distance between two stations to compensate for geometrical spreading. [Figure 13](#) summarizes the result for the four periods for which we showed tomographic maps ([Fig. 11](#)). For each station-pair, two arrows with opposite directions are plotted on both stations. The length of the arrow is proportional to the SNR multiplied by square root of the distance and the direction of the arrow represents the direction of wave propagation. Here we restrict the calculation to the station-pairs with distance in km larger than 6 times the period in second instead of 12 times used in the first selection criterion discussed in section 3.

Several conclusions can be drawn from these maps. At 8 and 13 sec period, the South Island has stronger coherent signals than the North Island. The signals at 8 sec

dominantly arrive from the south, southwest and southeast compared to the more azimuthally uniform signals observed on the North Island. Waves arriving from the north at short periods are very weak on the South Island. This is consistent with a previous study that the north coast has a low energy lee shore (REFERENCE?). At 13, 18, and 23 sec, stations TOZ, KNZ and WHZ have only very weak signals and appear to suffer from high local noise after an ambient noise level analysis was performed (e.g., Lin et al., 2006). For periods above 13 sec, strong waves are arriving both from the north and south. The signals, however, tend to be oriented mostly northeast-southwest along the strike of the islands, particularly on the South Island.. Part of the reason is that longer periods necessitate longer paths. It is, therefore, more difficult at the longer periods to infer the azimuthal distribution of the incoming waves. For this reason, we believe that only the 8 sec map adequately represents the azimuthal strength of incoming waves. Clearly, strong waves arrive between many stations at periods above 13 sec, but we cannot rule out strong waves at azimuths that are effectively unsampled by the station distribution.

## **6. Discussion**

### **6.1 Shear velocity models consistent with the observed dispersion curves**

### **6.2 Geological correlation of the group velocity maps**

## **7. Conclusions**



## **Acknowledgments**

The authors would like to thank the New Zealand GeoNet Project and the IRIS Data Management Center for the data on which this research is based.

## References

- Baldock, G. and T. Stern, 2005. Width of mantle deformation across a continental transform: Evidence from upper mantle (Pn) seismic anisotropy measurements, *Geology*, **33**(9), 741–744.
- Barmin, M.P., M.H. Ritzwoller, and A.L. Levshin, 2001. A fast and reliable method for surface wave tomography, *Pure Appl. Geophys.*, **158**, 1351 - 1375.
- Bensen, G.D., M.H. Ritzwoller, N.M. Shapiro, A.L. Levshin, 2005. Extending ambient noise surface wave tomography to continental scales: Application across the United States, *EOS Trans. AGU*, **86**(52), Fall Meeting Suppl., Abstract S31A-0274.
- Bensen, G.D., M.P. Barmin, A.L. Levshin, F.-C. Lin, M.P. Moschetti, N.M. Shapiro, Y. Yang, and M.H. Ritzwoller, 2006. Processing ambient noise seismic data to obtain reliable broad-band surface wave dispersion measurements, manuscript in preparation.
- Cho, K.H., R.B. Hermann, C.J. Ammon, and K. Lee, 2006. Imaging the upper crust of the Korean Peninsula by surface-wave tomography, *Bull. Seism. Soc. Amer.*, submitted.
- Campillo M. and A. Paul, 2003. Long-range correlations in the diffuse seismic coda, *Science*, **299**, 547-549.
- Dahlen, F.A. and Y. Zhou, 2006. Surface wave group delay and attenuation kernels, *Geophys. J. Int.*, in press.
- Davey, F.J., et al., 1998. Preliminary results from a geophysical study across a modern continent-continent collisional plate boundary — The Southern Alps, New Zealand, *Tectonophys.*, **288**, 221–235.
- Derode, A., E. Larose, M. Tanter, J. de Rosny, A. Tourim, M. Campillo, and M. Fink, 2003. Recovering the Green's function from field-field correlations in an open scattering medium (L), *J. Acoust. Soc. Am.*, **113**, 2973-2976.
- Larose, E., A. Derode, M. Campillo, and M. Fink, 2004. Imaging from one-bit correlations of wideband diffuse wavefields, *J. Appl. Phys.*, **95**, 8393-8399.
- Larose, E., A. Derode, D. Corenec, L. Margerin, and M. Campillo, 2005. Passive retrieval of Rayleigh waves in disordered elastic media, *Phys. Rev. E.*, **72**, 046607, doi:10.113/PhysRevE.72.046607.
- Levshin, A.L. and M.H. Ritzwoller, 2001. Automated detection, extraction, and measurement of regional surface waves, *Pure Appl. Geophys.*, **158**, 1531-1545.
- Levshin, A.L., M.P. Barmin, M.H. Ritzwoller, and J. Trampert, 2005. Minor-arc and major-arc global surface wave diffraction tomography, *Phys. Earth Planet. Ints.*, **149**, 205-223.
- Lin, F., M.H. Ritzwoller, and N.M. Shapiro, Is ambient noise tomography across ocean

- basins possible?, *Geophys. Res. Lett.*, in press.
- Okaya, D., S. Henrys, and T. Stern, 2002. Double-sided onshore-offshore seismic imaging of a plate boundary: "super-gathers" across South Island, New Zealand, *Tectonophys.*, **355**(1-4), 247–263.
- Paul, A., M. Campillo, L. Margerin, E. Larose, and A. Derode, 2005. Empirical synthesis of time-asymmetrical Green functions from the correlation of coda waves, *J. Geophys. Res.*, **110**, B08302, doi:10.1029/2004JB003521.
- Reyners, M., et al., 2006. Imaging subduction from the trench to 300 km depth beneath the central North Island, New Zealand, with Vp and Vp/Vs, *Geophys. J. Int.*, **165**(2), 565-583.
- Ritzwoller, M. H. and A. L. Levshin, 1998. Eurasian surface wave tomography: group velocities, *J. Geophys. Res.*, **103**, 4839-4878.
- Ritzwoller, M.H., Shapiro, N.M., Barmin, M.P., & Levshin, A.L., 2002. Global surface wave diffraction tomography, *J. Geophys. Res.*, **107**, B12, 10.1029/2002JB001777.
- Roux, P., K.G. Sabra, P. Gerstoft, W.A. Kuperman, and M.C. Fehler, 2005. P-waves from cross-correlation of seismic noise, *Geophys. Res. Lett.*, **32**, L19393, doi:10.1029/2005GL023803.
- Sabra, K. G., P. Gerstoft, P. Roux, W. A. Kuperman, and M. C. Fehler 2005a. Extracting time-domain Green's function estimates from ambient seismic noise, *Geophys. Res. Lett.*, **32**, L03310, doi:10.1029/2004GL021862.
- Sabra, K. G., P. Gerstoft, P. Roux, W. A. Kuperman, and M. C. Fehler 2005b. Surface wave tomography from microseism in southern California, *Geophys. Res. Lett.*, **32**, L14311, doi:10.1029/2005GL023155.
- Savage, M.K., K.M. Fisher, and C.E. Hall, 2004. Strain modelling, seismic anisotropy, and coupling at strike-slip boundaries: applications in New Zealand and the San Andreas fault, in *Vertical coupling and decoupling in the lithosphere*, J. Grocott, et al., Editors, Geological Society, London, p. 9–40.
- Scherwath, M., et al., 2002. Pn anisotropy and distributed upper mantle deformation associated with a continental transform fault, *Geophys. Res. Lett.*, **29**(8), 16–1.
- Shapiro, N.M. and M. Campillo, 2004. Emergence of broadband Rayleigh waves from correlations of the ambient seismic noise, *Geophys. Res. Lett.*, **31**, L07614, doi:10.1029/2004GL019491.
- Shapiro, N.M. and M.H. Ritzwoller, 2002. Monte-Carlo inversion for a global shear velocity model of the crust and upper mantle, *Geophys. J. Int.*, **151**, 88-105.
- Shapiro, N.M. M. Campillo, L. Stehly, and M.H. Ritzwoller, 2005. High resolution surface wave tomography from ambient seismic noise, *Science*, **307**, 1615-1618.

- Sieminski, A., J.-J. Leveque, and E. Debayle, 2004. Can finite-frequency effects be accounted for in ray theory surface wave tomography?, *Geophys. Res. Lett.*, **31**, L24614, doi:10.1029/2004GL021402.
- Snieder, R., 2004. Extracting the Green's function from the correlation of coda waves: A derivation based on stationary phase, *Phys. rev. E*, **69**, 046610.
- Spetzler, J., Trampert, J. & Snieder, R., 2002. The effects of scattering in surface wave tomography, *Geophys. J. Int.*, **149**,755-767.
- Stern, T., et al., 2000. Teleseismic P wave delays and modes of shortening the mantle lithosphere beneath South Island, New Zealand, *J. Geophys. Res.*, **105**(B9), 21615–21631.
- Stern, T., 2006. Subduction at a continental margin: kinematics and dynamics of the central North Island, New Zealand, *Revs. Geophys.*, in press.
- Wapenaar, K., 2004. Retrieving the elastodynamic Green's function of an arbitrary inhomogeneous medium by cross correlation, *Phys. Rev. Lett.*, **93**, 254301, doi:10.1103/PhysRevLett.93.254301.
- Weaver, R.L. and O. I. Lobkis, 2001a. Ultrasonics without a source: Thermal fluctuation correlation at MHz frequencies, *Phys. Rev. Lett.*, **87**, paper 134301.
- Weaver, R.L. and O.I. Lobkis, 2001b. On the emergence of the Green's function in the correlations of a diffuse field, *J. Acoust. Soc. Am.*, **110**, 3011-3017.
- Weaver, R.L. and O.I. Lobkis, 2004. Diffuse fields in open systems and the emergence of the Green's function, *J. Acoust. Soc. Am.*, **116**, 2731-2734.
- Yao, H., R.D. van der Hilst, and M. V. de Hoop, 2006. Surface-wave tomography in SE Tibet from ambient seismic noise and two-station analysis: I. – Phase velocity maps, *Geophys. J. Int.*, submitted.
- Yoshizawa, K. & Kennett, B. L. H., 2002. Determination of the influence zone for surface wave paths, *Geophys. J. Int.*, **149**,440-453.
- Zhou Y., Dahlen, F.A. & Nolet, G., 2004. 3-D sensitivity kernels for surface-wave observables, *Geophys. J. Int.*, **158**, 142-168.

## Figure Captions

**Figure 1.** The stations used in this study: 41 stations from the New Zealand GeoNet Project and one (SNZO) from the Global Seismic Network (Butler et al., 2004).

**Figure 2.** A broad-band (5 - 150 sec period) record section centered at station BFZ (???????, New Zealand). Both positive (“causal”) and negative (“acausal”) lags are shown. The grey-lines mark a “move-out” of 2 km/sec and 3 km/sec.

**Figure 3.** One-year stack of the symmetric component cross-correlation signal observed for the station-pair DSZ-HIZ (???????, ??????????) filtered into various pass-bands.

**Figure 4.** (a) A one-year cross-correlation between stations EAZ (???????) and THZ (???????) showing the window defining the signal location outlined in red. The cross-correlation is the top waveform and the symmetric-component waveform is shown below it. (b) The spectrum of the signal-to-noise ratio of the positive and negative lags of the cross-correlation and the symmetric-component shown in (a). (c) Frequency-time image of the symmetric-component shown in (a) and the measured raw group-speed

curve where warm colors indicate large amplitudes. (d) Frequency-time image after phase-matched filtering based on the raw dispersion measurement. The black line is the raw dispersion measurement from (c), the magenta line is the group speed measurement from phase-matched filtering, and the vertical blue line is the cut-off period; below this period waves travel more than 3 wavelengths between the stations.

**Figure 5.** (a) Inter-station paths for the group speed measurements shown in (b). Paths through: an off-shore basin (OUZ-QRZ), the Southern Alps (DCZ-LTZ), the eastern side of the South Island (KHZ-ODZ), and the North island (PXZ-WCZ). Color codes on (a) and (b) are the same.

**Figure 6.** The measured group speed curves for twelve 3-month stacks are shown by red-lines and the curve for the one-year is shown with a black curve for the station-pair THZ (????????) and TUZ (????????). The variation between the measurements of three-month stacks are used to estimate measurement uncertainties.

**Figure 7.** The average STD of group speed for each period is shown. For a period covered by more than one period band, the period band with lowest average STD was

chosen to provide the group velocity measurement.

**Figure 8.** (a) The total number of group speed measurements at each period after completion of data selection. (b) The average of SNR across all accepted measurements for each period. (c) The average of the standard deviation (STD) of the group speed measurements among the three-month for each period. This is interpreted as the average measurement uncertainty. (d) Same as (c), but this panel quantified the uncertainty in arrival times.

**Figure 9.** The inter-station paths are shown for all of the group speed measurements that pass the selection criteria at periods of 8, 13, 18, and 23 sec.

**Figure 10.** Estimated resolution at periods of 8, 13, 18, and 23 sec. Resolution is defined as the standard deviation of the Gaussian fit to the resolution map at each model node (defined in km).

**Figure 11.** The estimated group velocity maps at periods of 8, 13, 18, and 23 sec.

**Figure 12.** Histograms of travel time misfit after tomography at periods of 8, 13, 18, and 23 sec.

**Figure 13.** Summary of the ambient noise directionality at periods of 8, 13, 18, and 23 sec. For each station pair separated by more than 1.5 wavelengths, two arrows with opposite directions are added to both stations. The length of each arrow is calculated from the SNR at positive or negative lag (whichever is directionally appropriate) multiplied by the square root of the inter-station distance. The directions of the arrows point along the great-circle linking the stations.



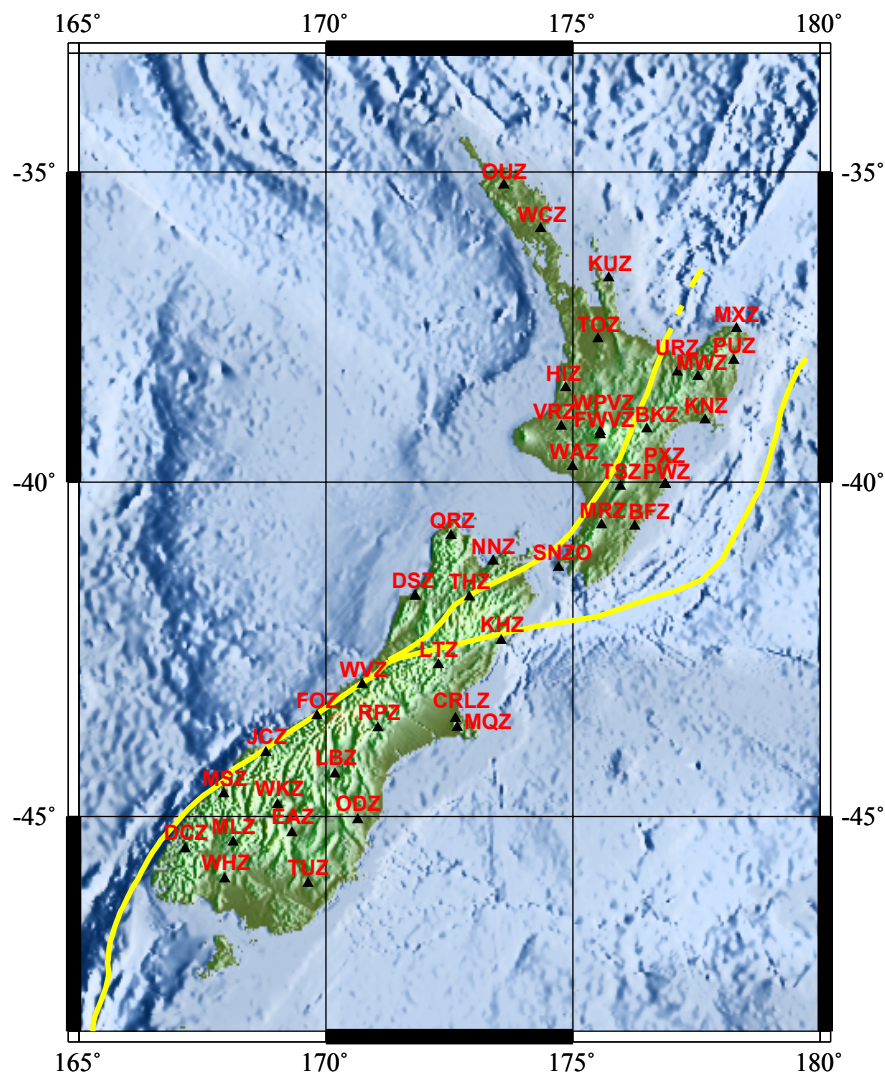


Fig. 1

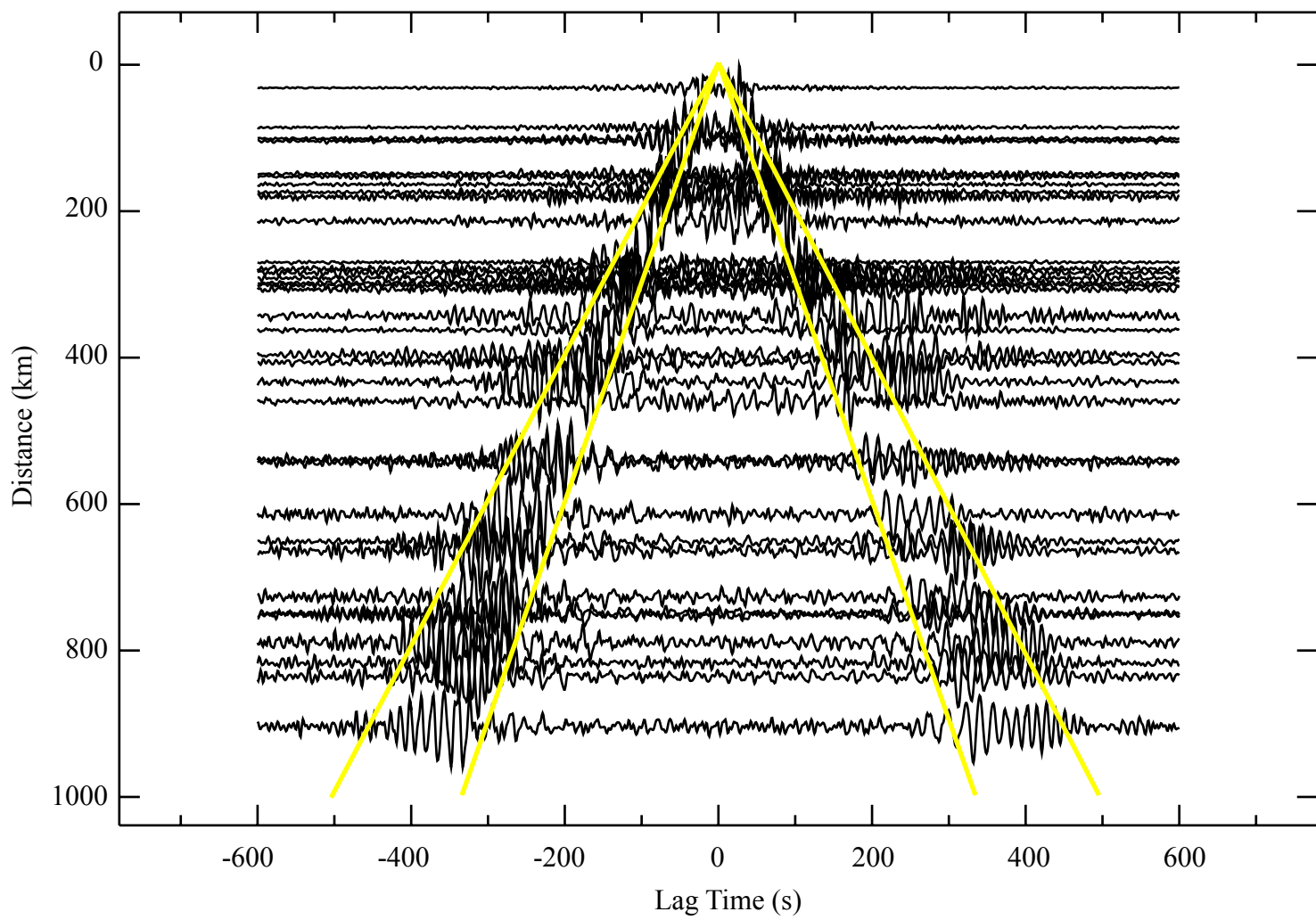


Fig. 2

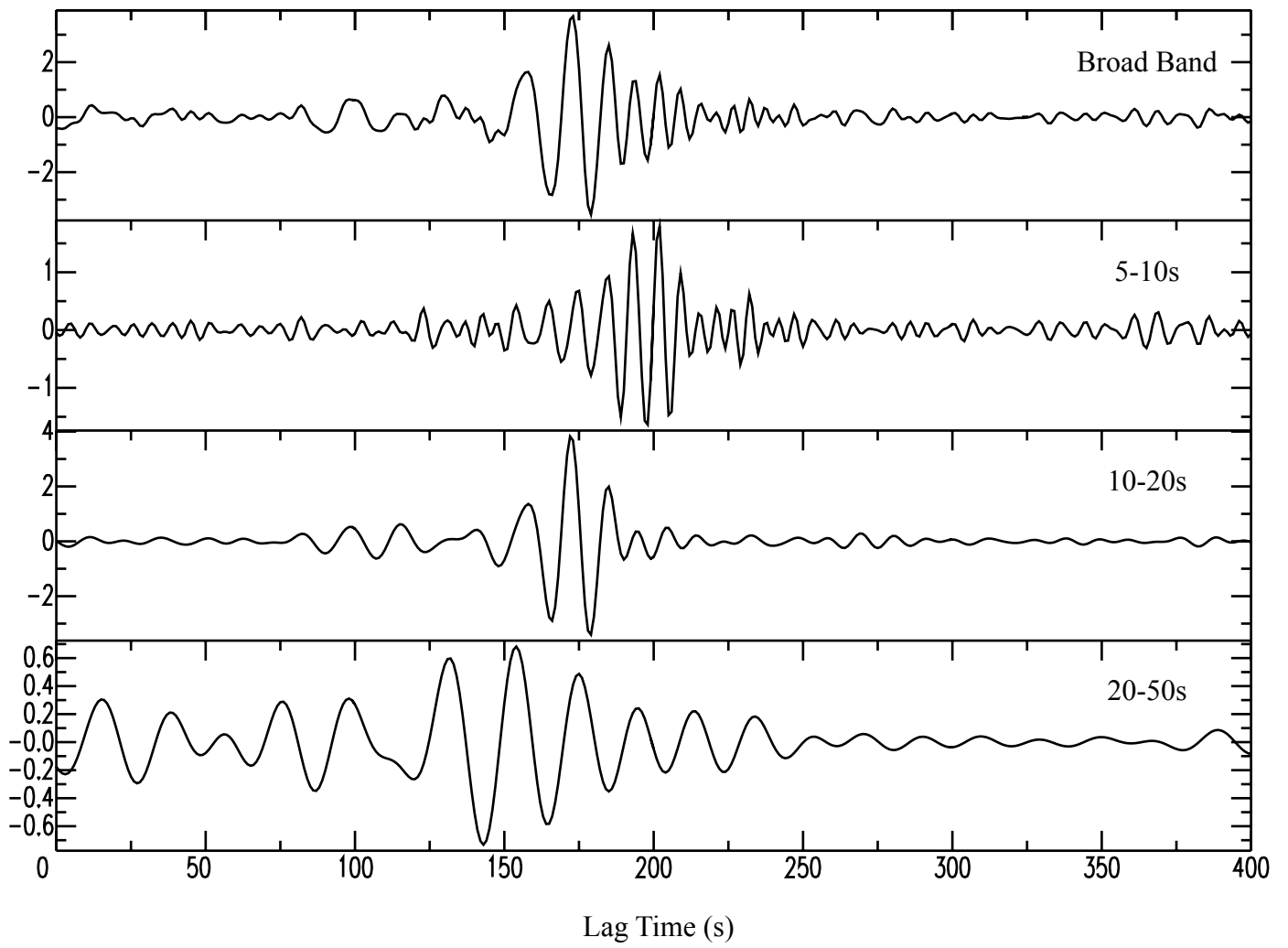


Fig.3

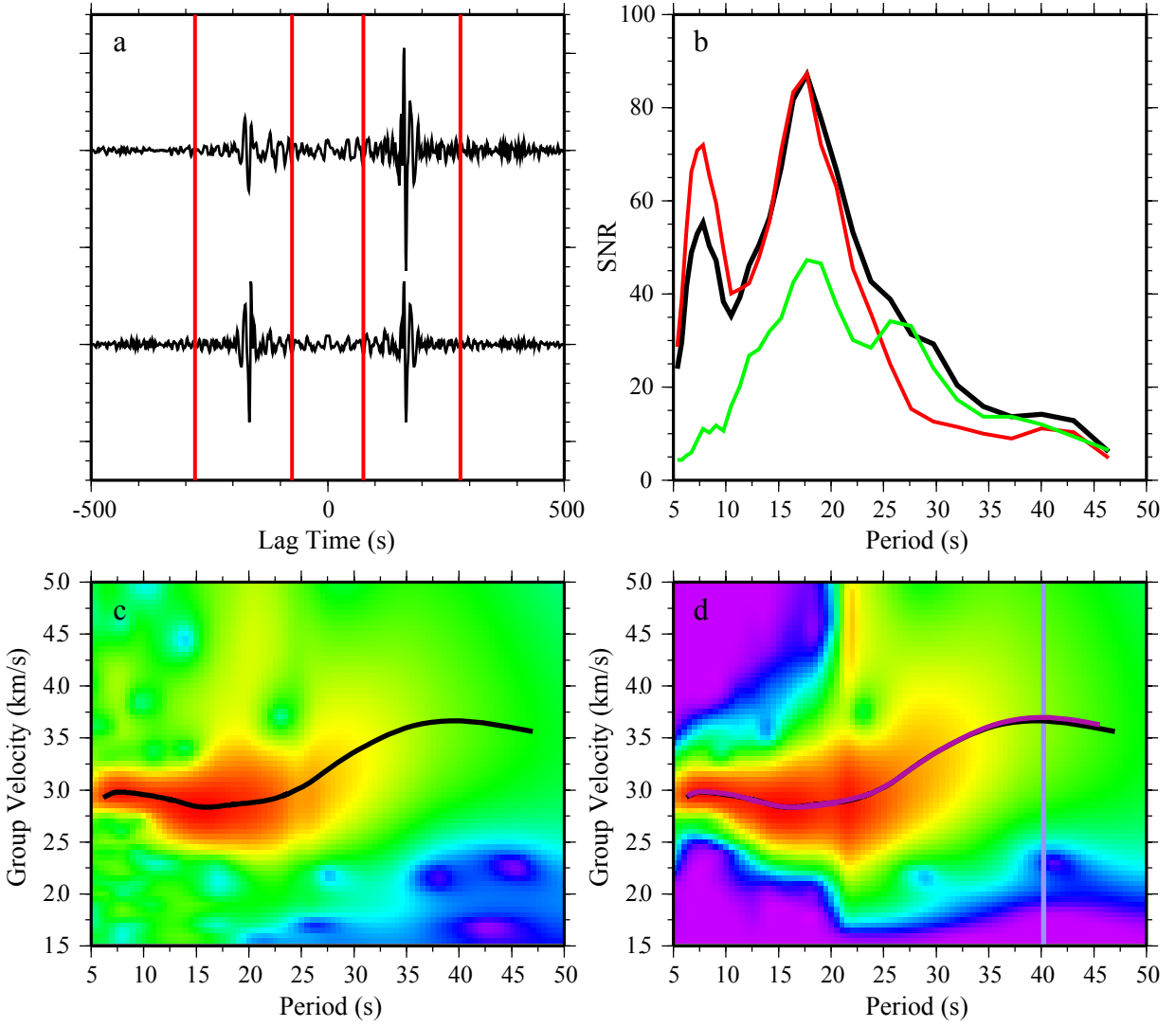
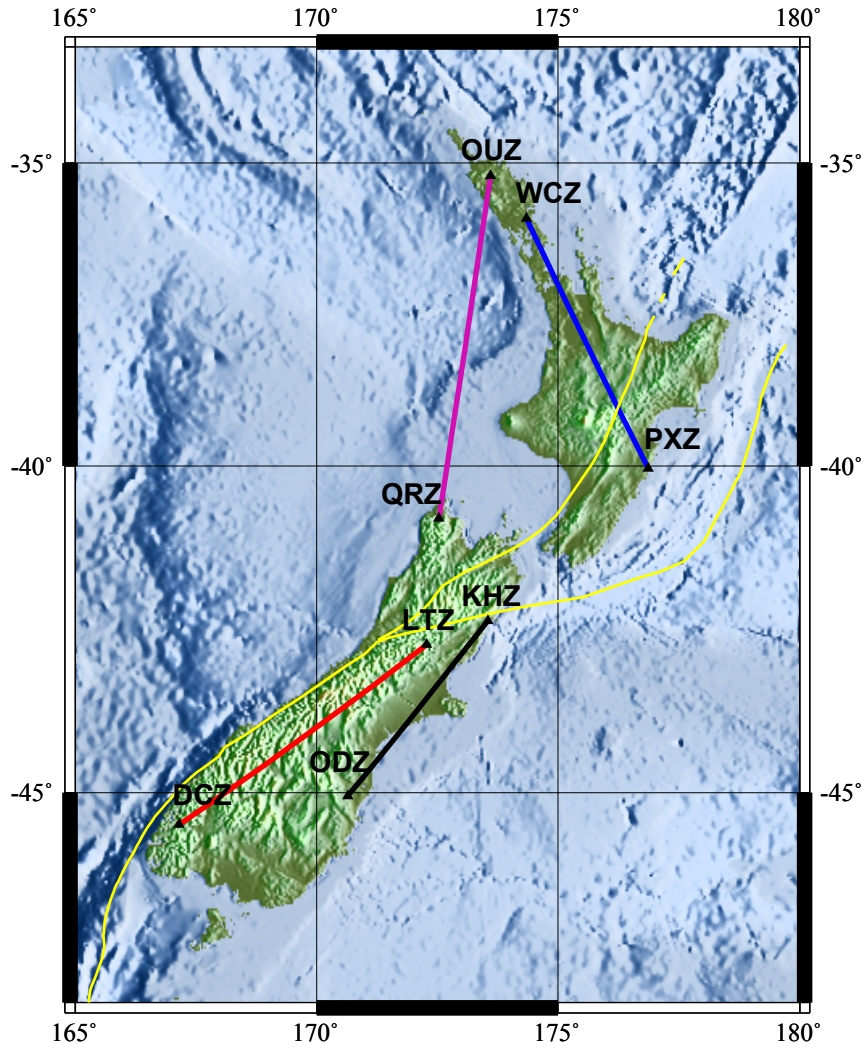


Fig. 4

a



b

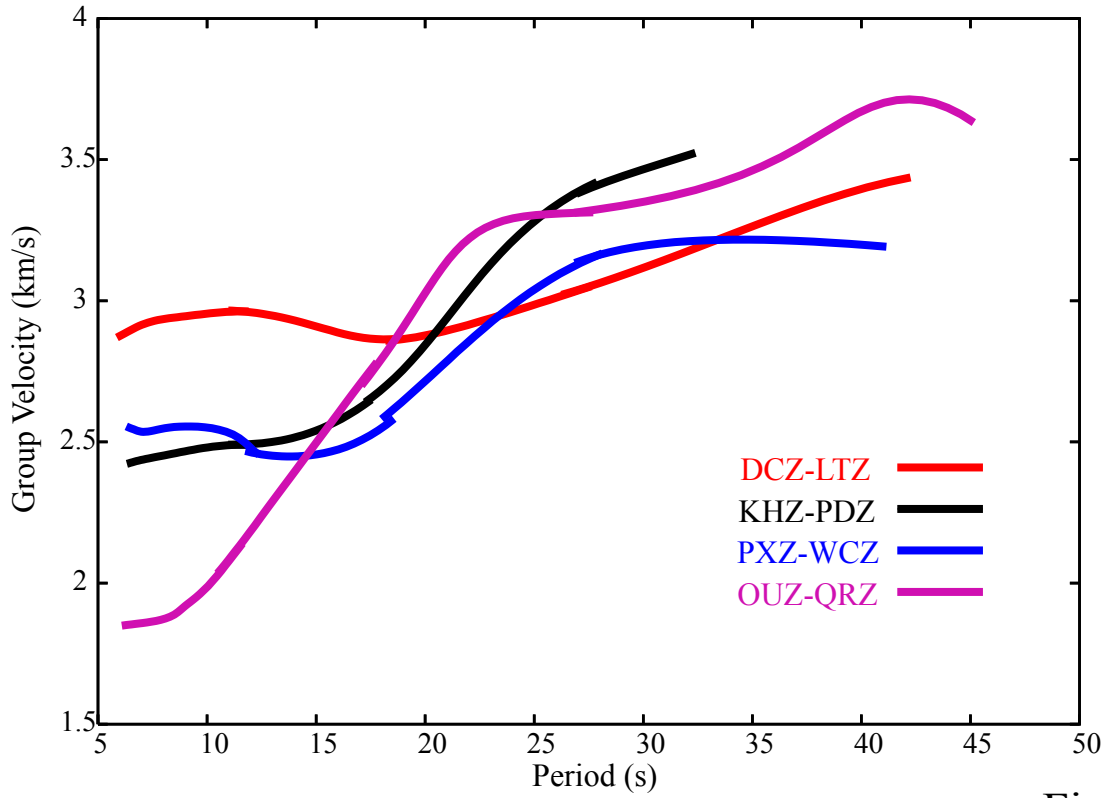


Fig. 5

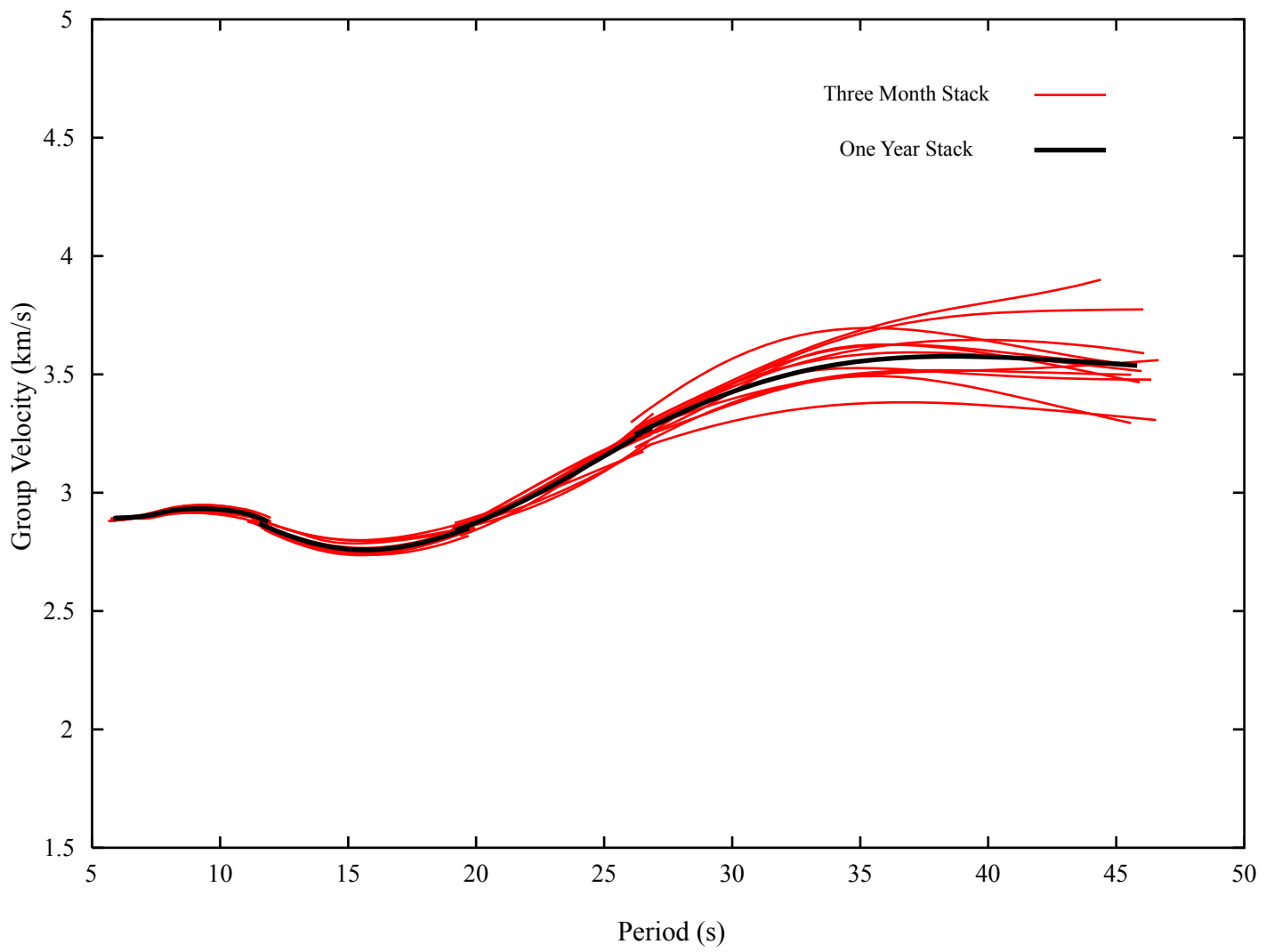


Fig. 6

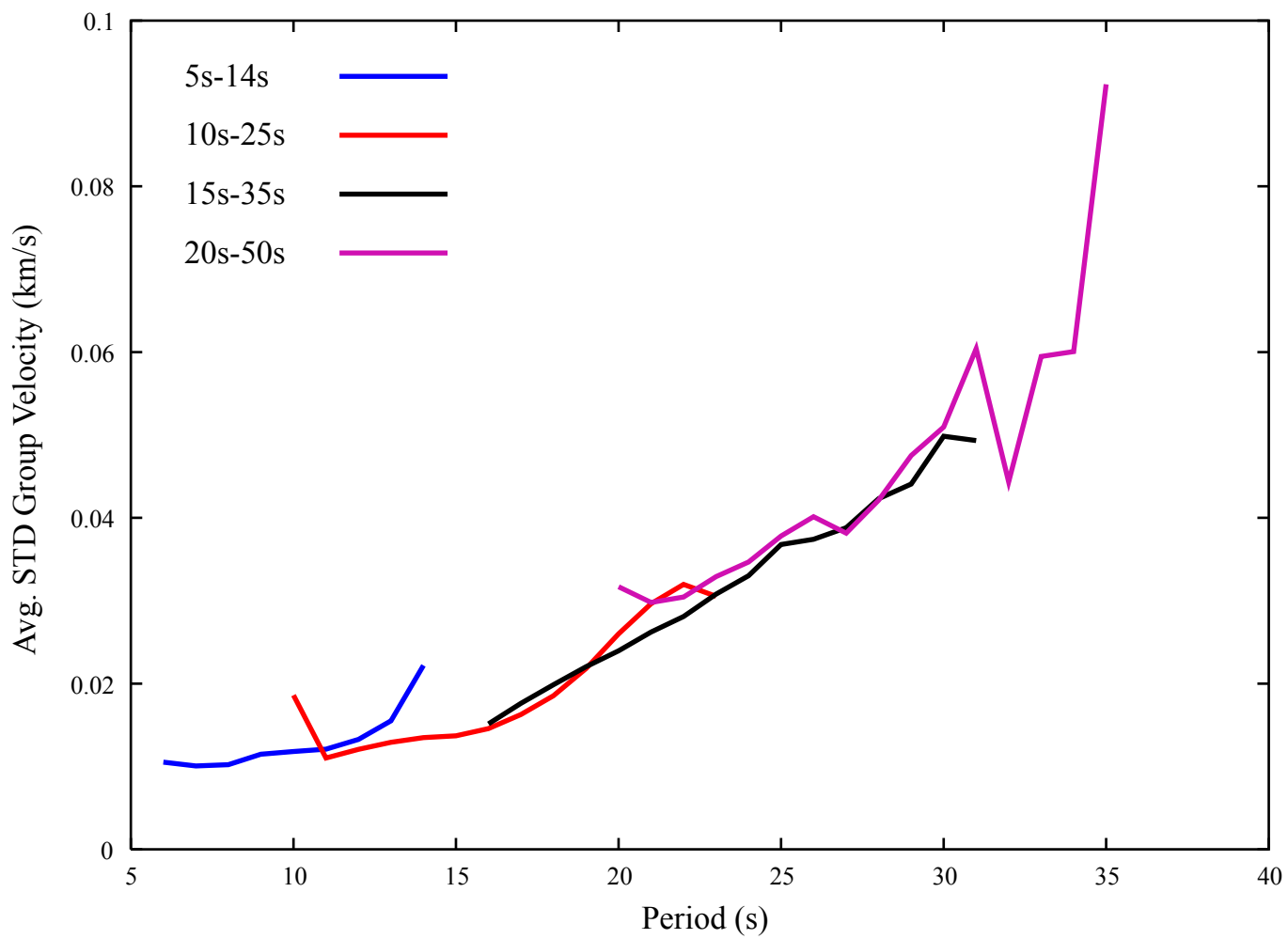


Fig. 7

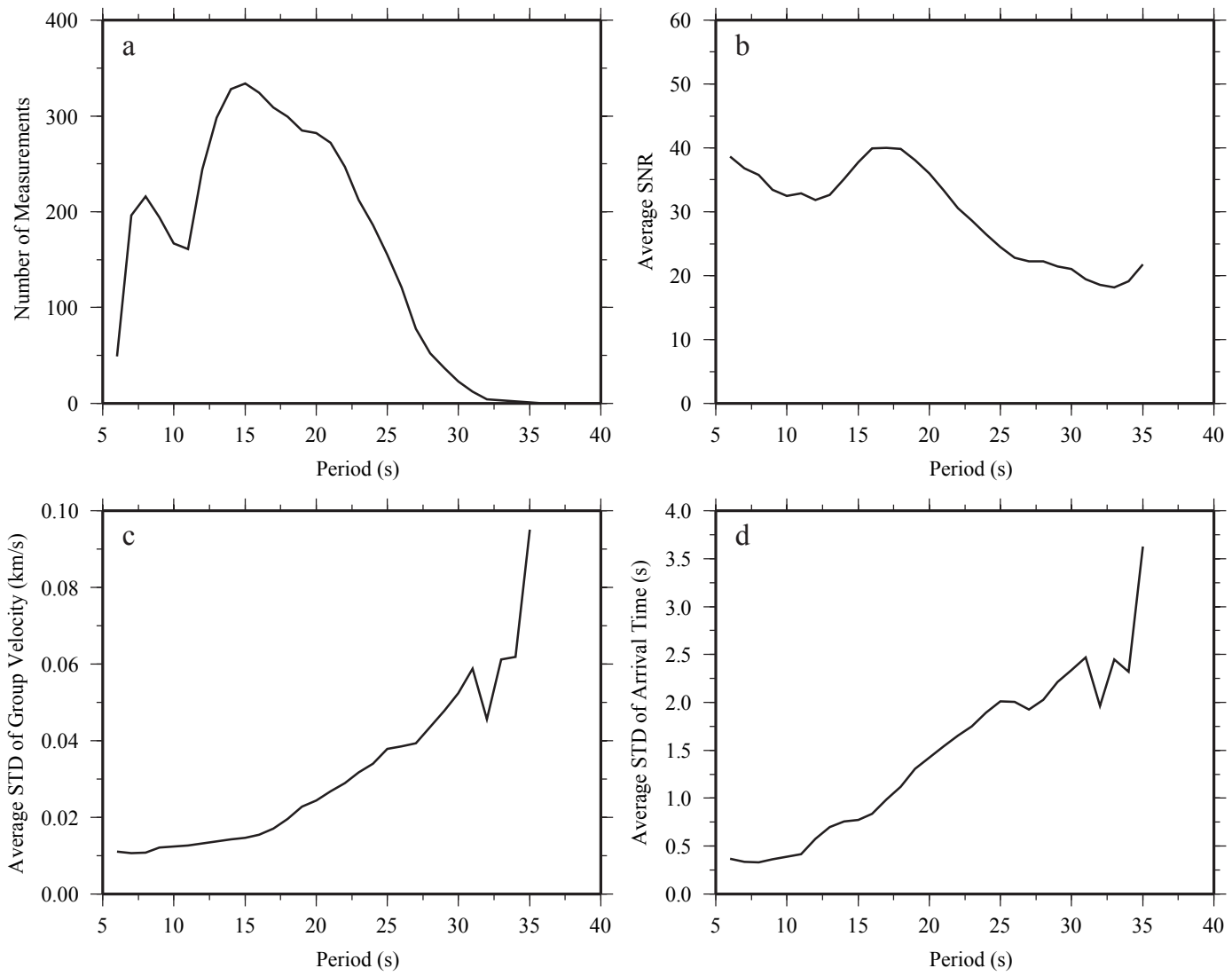


Fig.8



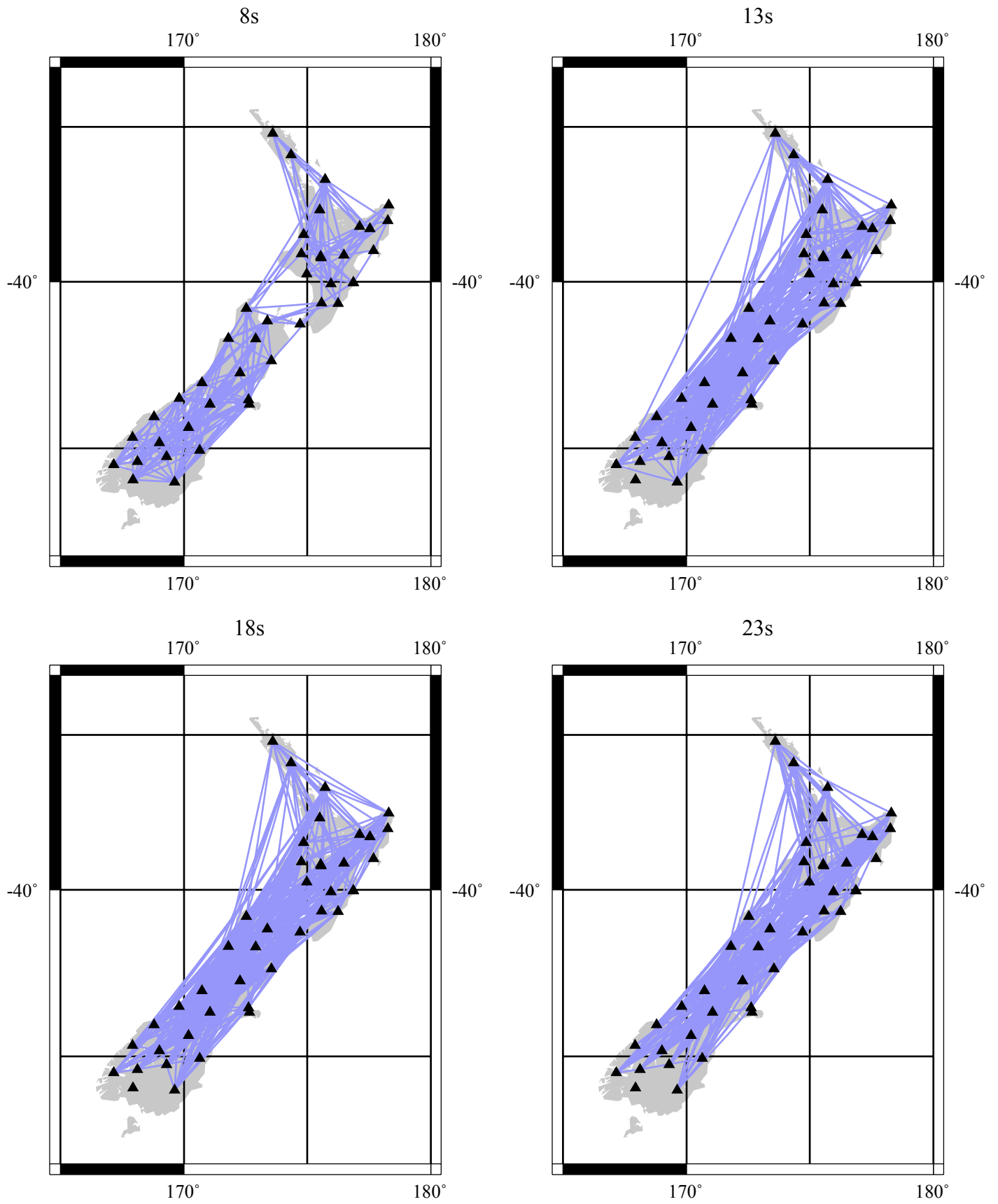


Fig. 9

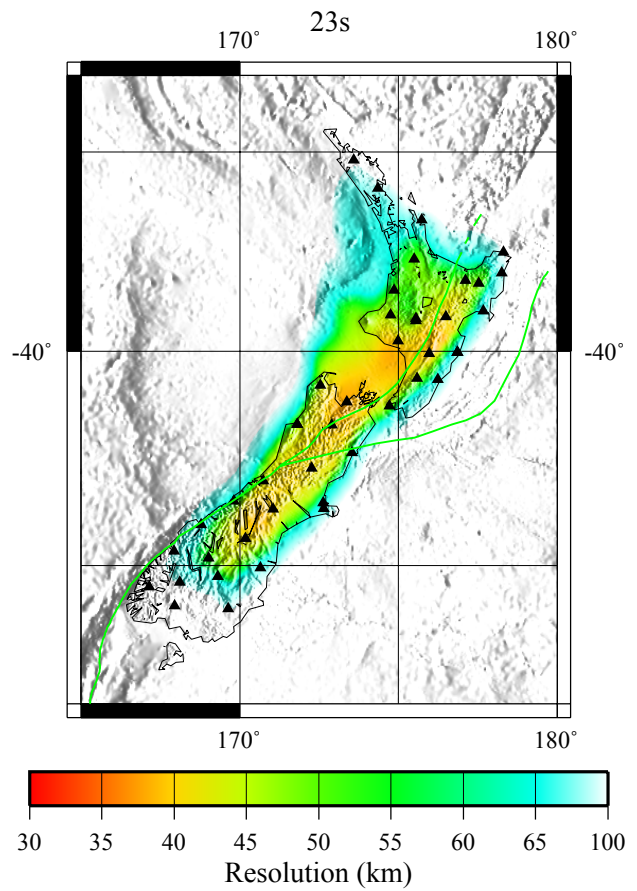
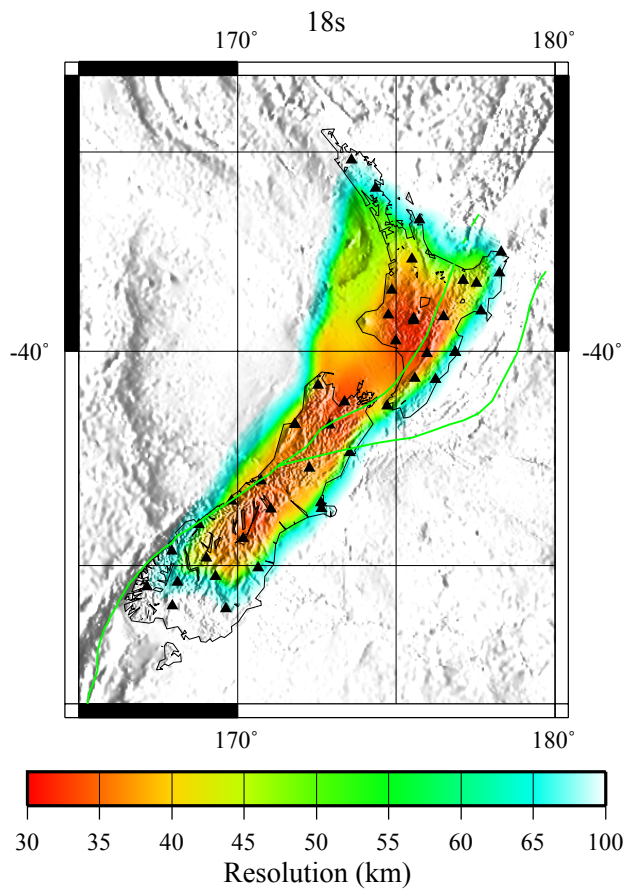
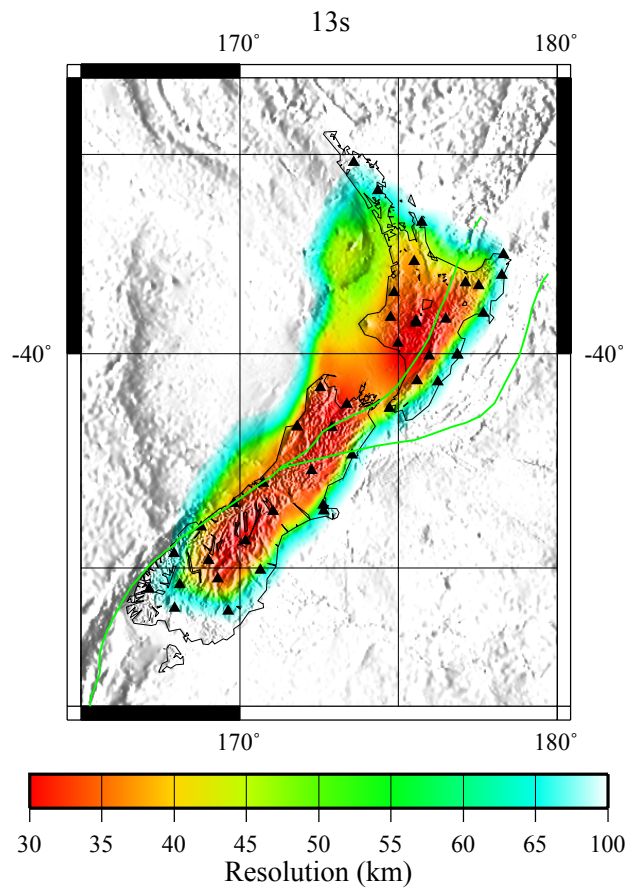
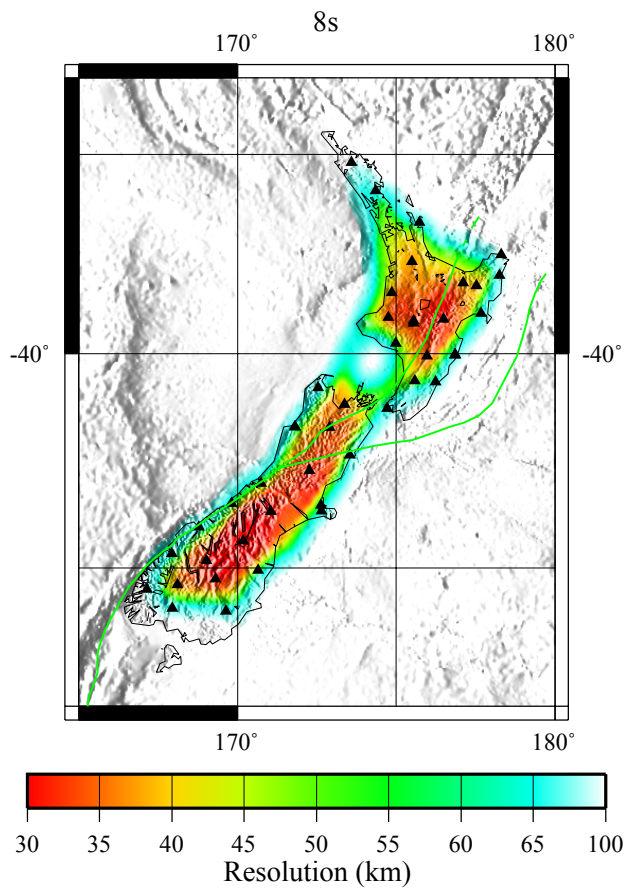


Fig.10

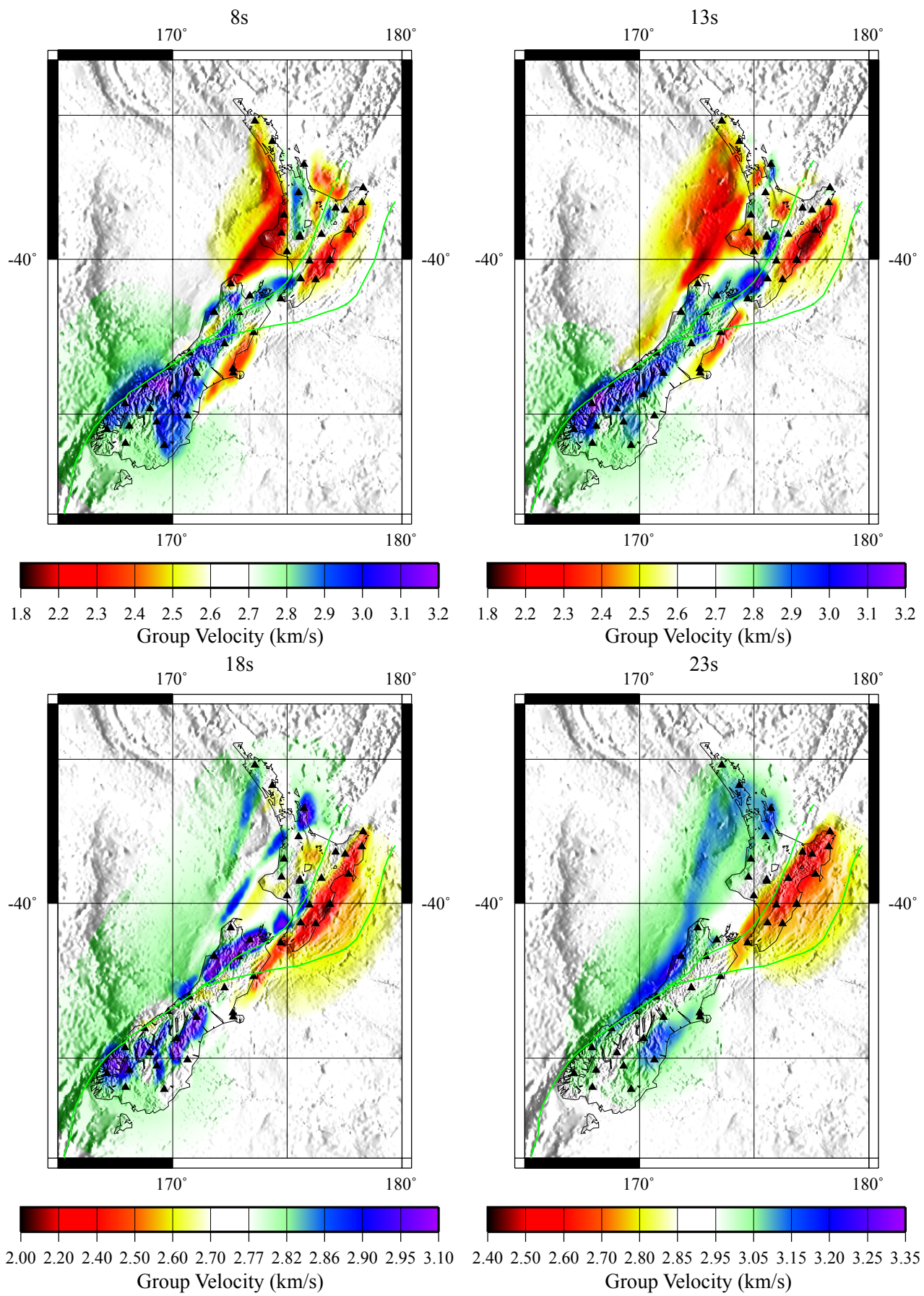


Fig. 11

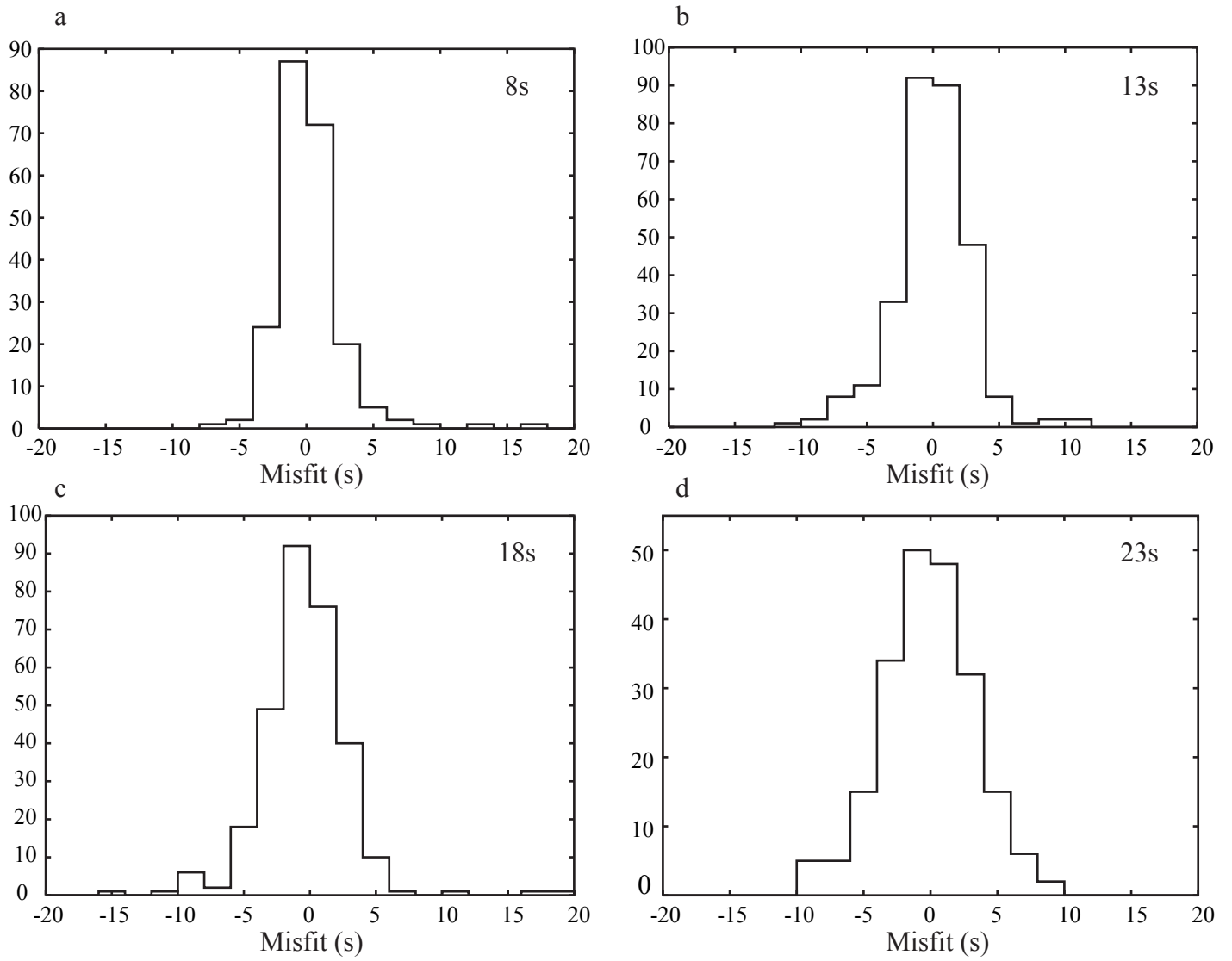


Fig. 12

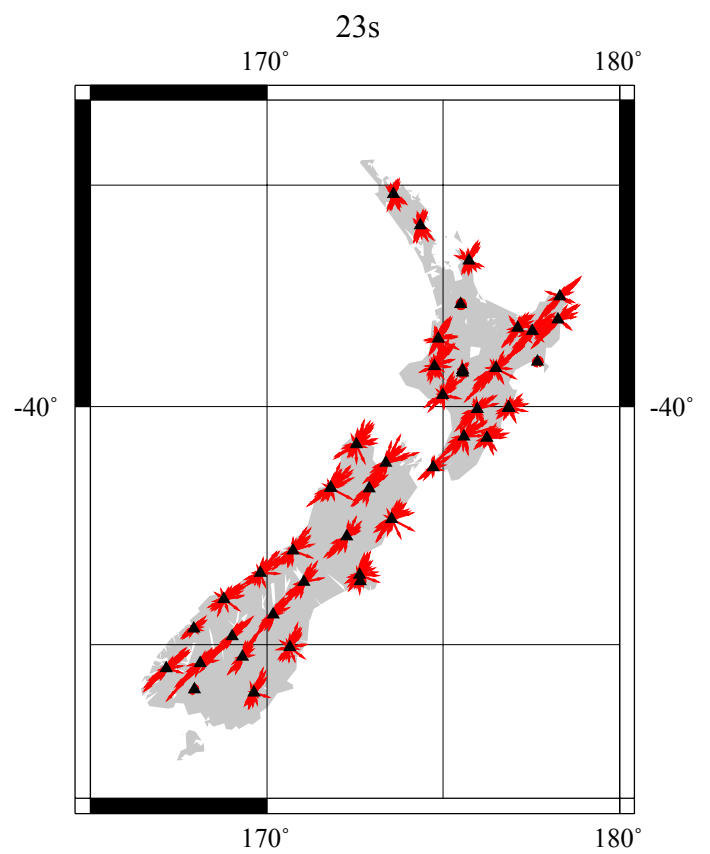
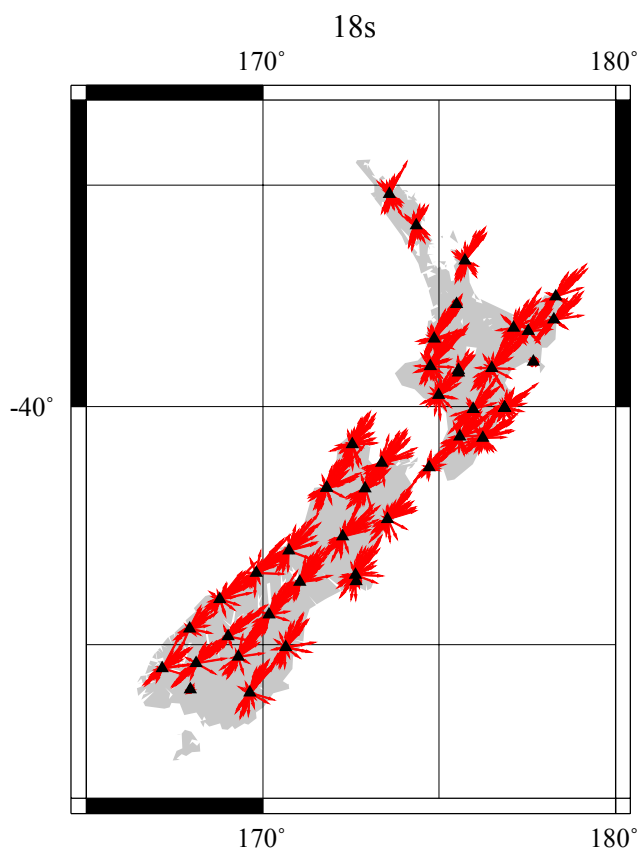
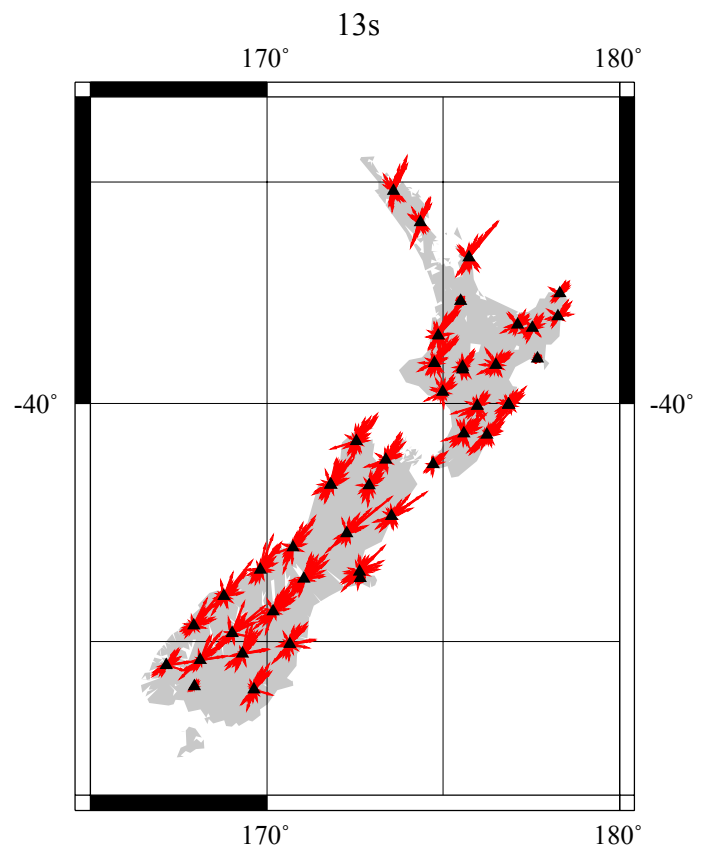
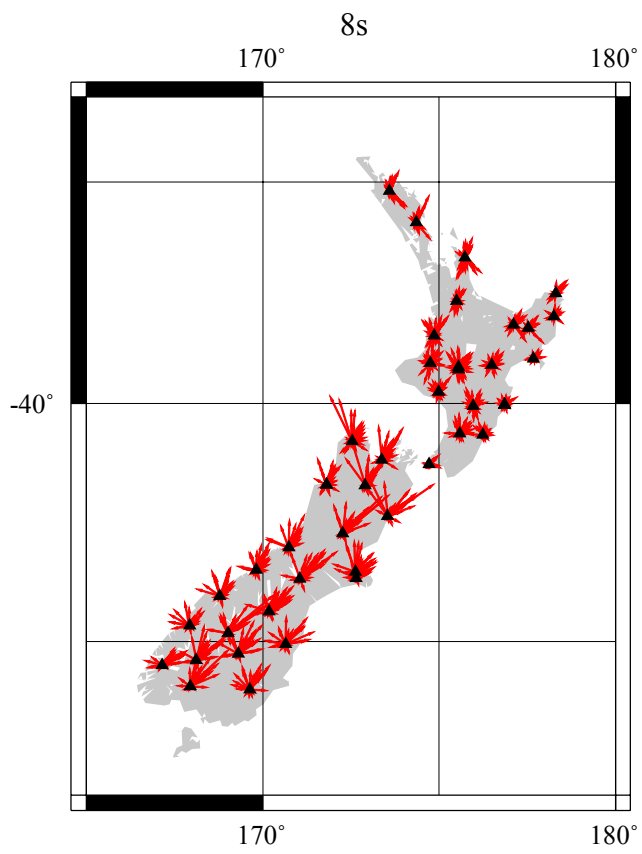


Fig. 13